# Supplementary Information

# Multifunctional CMOS-Integrable and Reconfigurable 2D Ambipolar Tellurene Transistors for Neuromorphic and In-Memory Computing

Bolim You[ab⊥], Jihoon Huh[ab⊥], Yuna Kim[a], Mino Yang[c], Unjeong Kim[*d], Min-Kyu Joo[*efg], Myung Gwan Hahm[*ah], Moonsang Lee[*ab]

[a] Department of Materials Science and Engineering, Inha University, 100 Inha-ro, Michuhol-gu, Incheon 22212, Republic of Korea

[b] Program in Semiconductor Convergence, Inha University, 100 Inha-ro, Michuhol-gu, Incheon 22212, Republic of Korea

[c] Korea Basic Science Institute Seoul, 6-7, Goryeodae-ro 22-gil, Seongbuk-gu, Seoul 02841, Republic of Korea

[d] Department of physics, Dongguk university, Seoul 04620, Republic of Korea

[e] Department of Applied Physics, Sookmyung Women's University, Seoul 04310, Republic of Korea

[f] Institute of Advanced Materials and Systems, Sookmyung Women's University, Seoul 04310, Republic of Korea

[g] Electrical Engineering Division, Engineering Department, University of Cambridge, Cambridge CB3 0FA, UK

[h] Institute for Bio-Medical and Translational Health Care, Inha University Hospital, 27 Inhang-ro, Jung-gu, Incheon 22332, Republic of Korea

* Corresponding authors.

E-mail addresses: ujjane.kim@dongguk.edu (U. Kim), mkjoo@sookmyung.ac.kr (M.-K. Joo), mghahm@inha.ac.kr (M.G. Hahm), mslee@inha.ac.kr (M. Lee)

┴Bolim You and Jihoon Huh contributed equally to this paper.

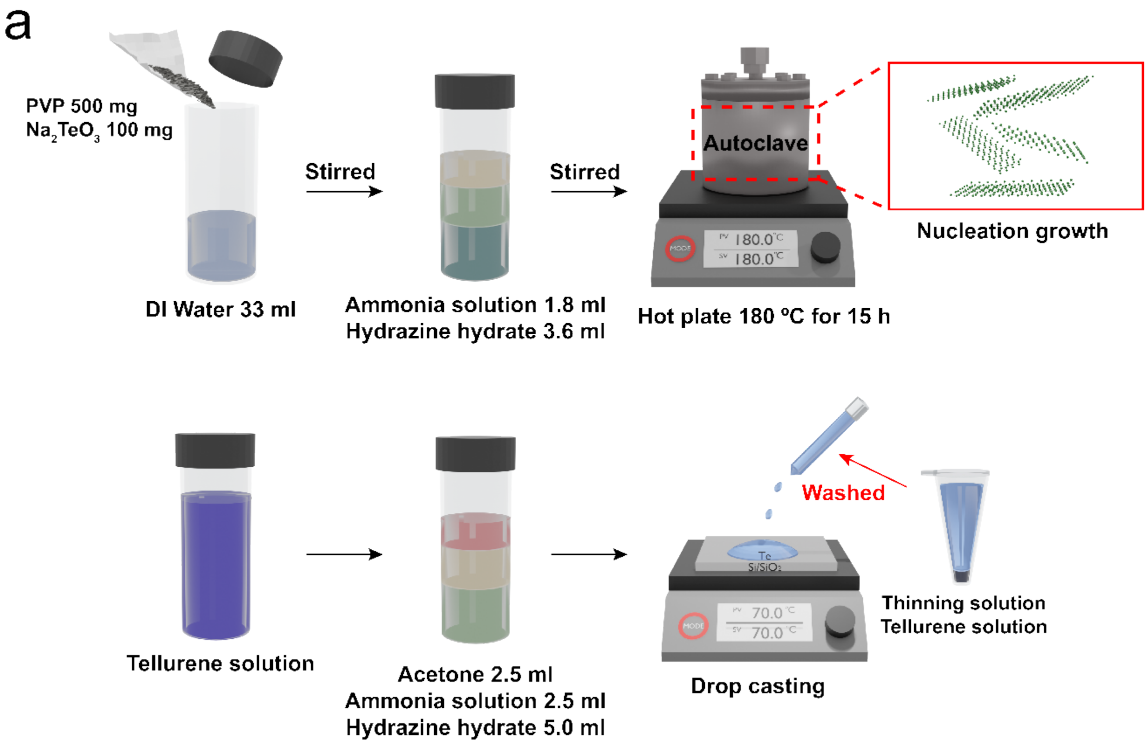


**Figure S1.** (a) Schematic of the hydrothermal process for synthesizing atomic-layered tellurene(Te) using solvent-assisted thinning.

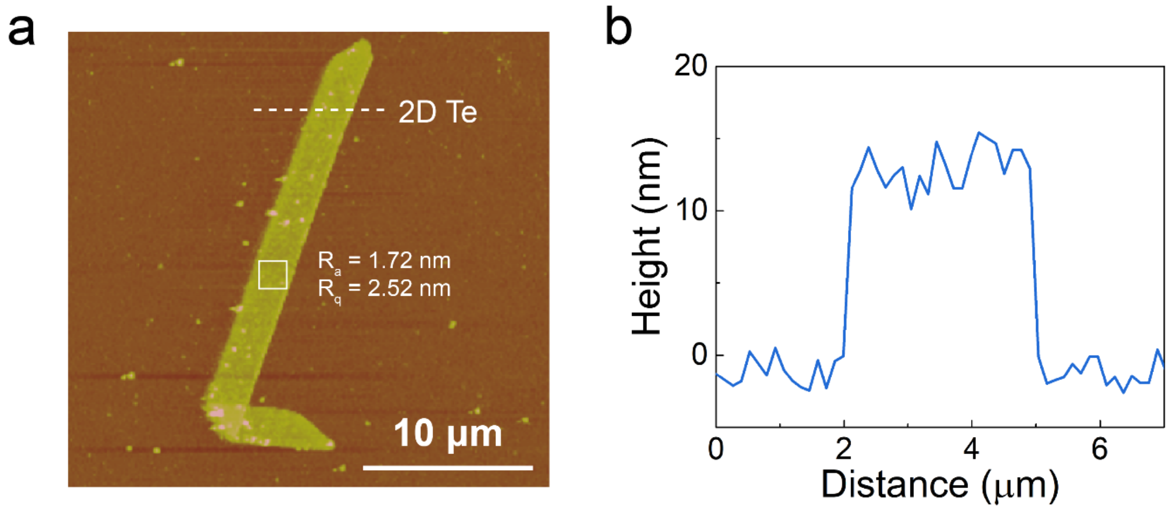


**Figure S2.** (a) Atomic force microscopy (AFM) image of a 2D Te nanoflake. The measured surface roughness values within the selected region are $R_a$ =1.72 nm and $R_q$ = 2.52 nm. (b) Corresponding height profile taken along the white dashed line, showing a thickness of approximately 13 nm for the 2D Te flake.

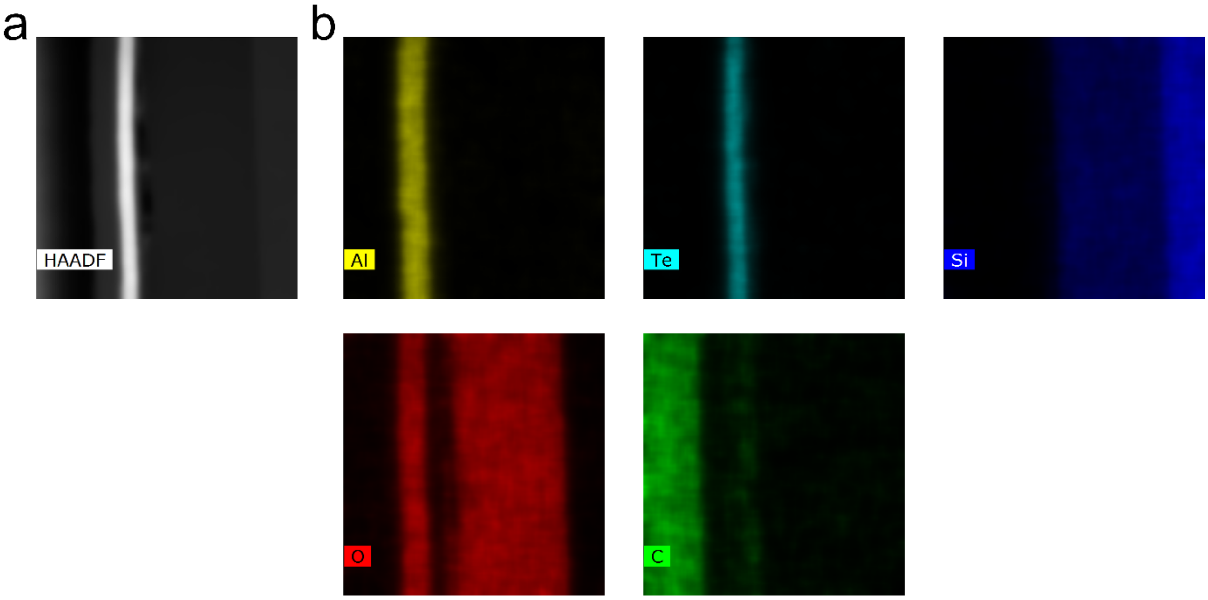


**Figure S3.** (a) High-angle annular dark-field scanning transmission electron microscopy (HAADF–STEM) image of Te on a Si/$SiO_2$ substrate with a 20 nm $Al_2O_3$ layer. (b) EDS mapping images of Al, Te, Si, O, and C.

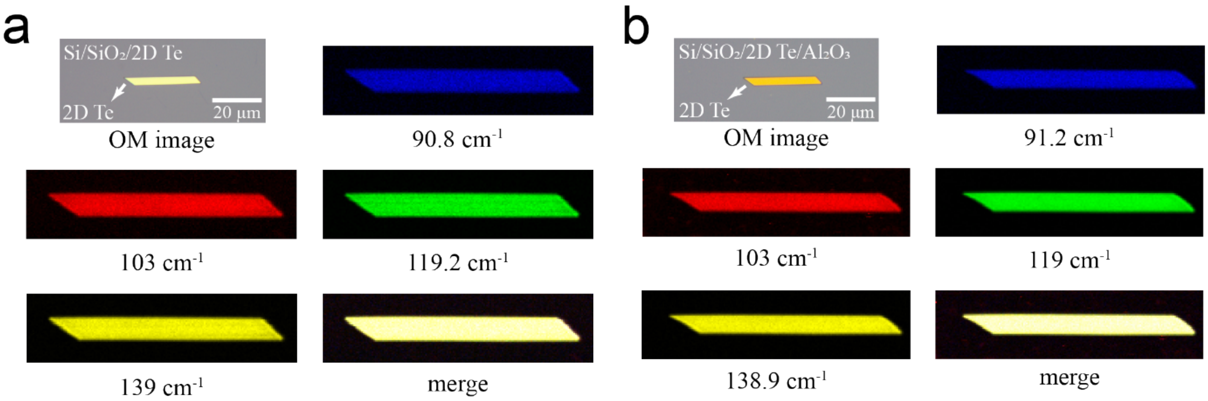


**Figure S4.** Optical and Raman mapping images of (a) bare 2D Te and (b) 2D Te with 20 nm $Al_2O_3$ on $Si/SiO_2$ (100 nm).

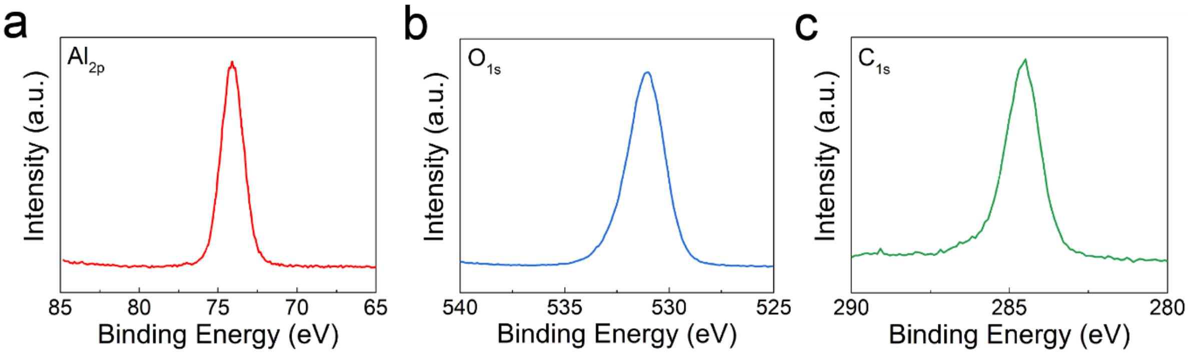


**Figure S5.** XPS core level spectra of (a) $Al_{2p}$, (b) $O_{1s}$, and (c) $C_{1s}$ for $Al_2O_3$ on 2D Te flake.

**Table S1.** Atomic percentage calculation for Al, O, and Te in $Al_2O_3$/Te. The obtained O/Al ratio of 1:1.45 indicates oxygen deficiency.

| | Peak Binding energy (eV) | Height CPS | FWHM (eV) | Area under curve | Atomic % |
|---|---|---|---|---|---|
| $Al_{2p}$ | 74.39 | 5546.3 | 1.67 | 10299.57 | 40.57 |
| $O_{1s}$ | 531.07 | 24581.16 | 2.07 | 57163.2 | 59.07 |
| $Te_{3d}$ | 576.6 | 300.33 | 3.75 | 4859.96 | 0.35 |

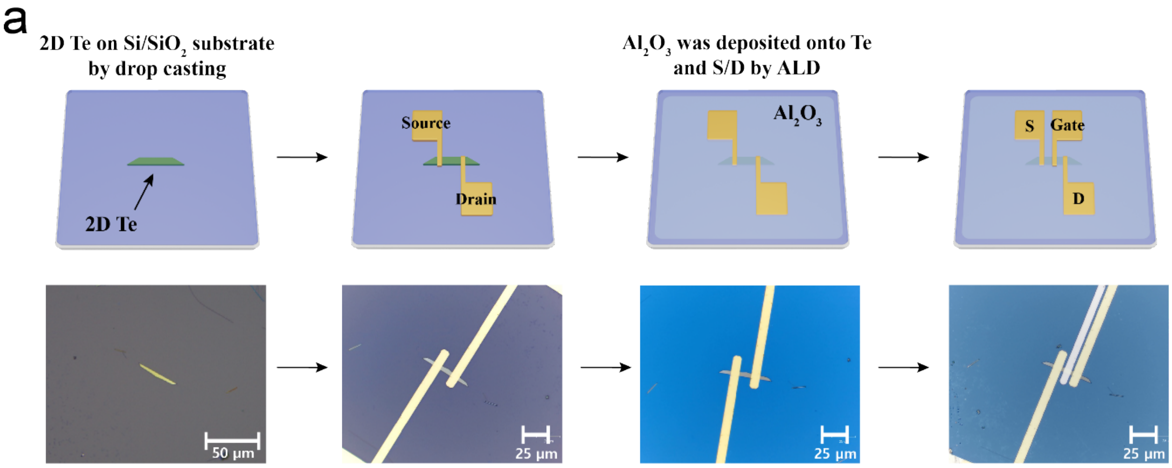


**Figure S6.** (a) Schematic and OM images of ambipolar 2D Te transistor fabrication method.

The source and drain electrodes with a channel length and width of 12 and 4.5 μm, respectively, were fabricated along the [0001] direction to consider the crystal anisotropy of the Te flake. All the electrodes, including the gate electrode, were fabricated employing conventional photolithography and e-beam evaporation. The electrodes were deposited at an evaporator chamber pressure of ~$10^{-5}$ Torr or lower, with a deposition rate of 1 Å/s, using Ti/Au (30 nm/70 nm). The $Al_2O_3$ thin film was deposited *via* thermal ALD following the fabrication of the source/drain electrodes to modulate the 2D Te from p-type to ambipolar while utilizing it as a gate dielectric layer.

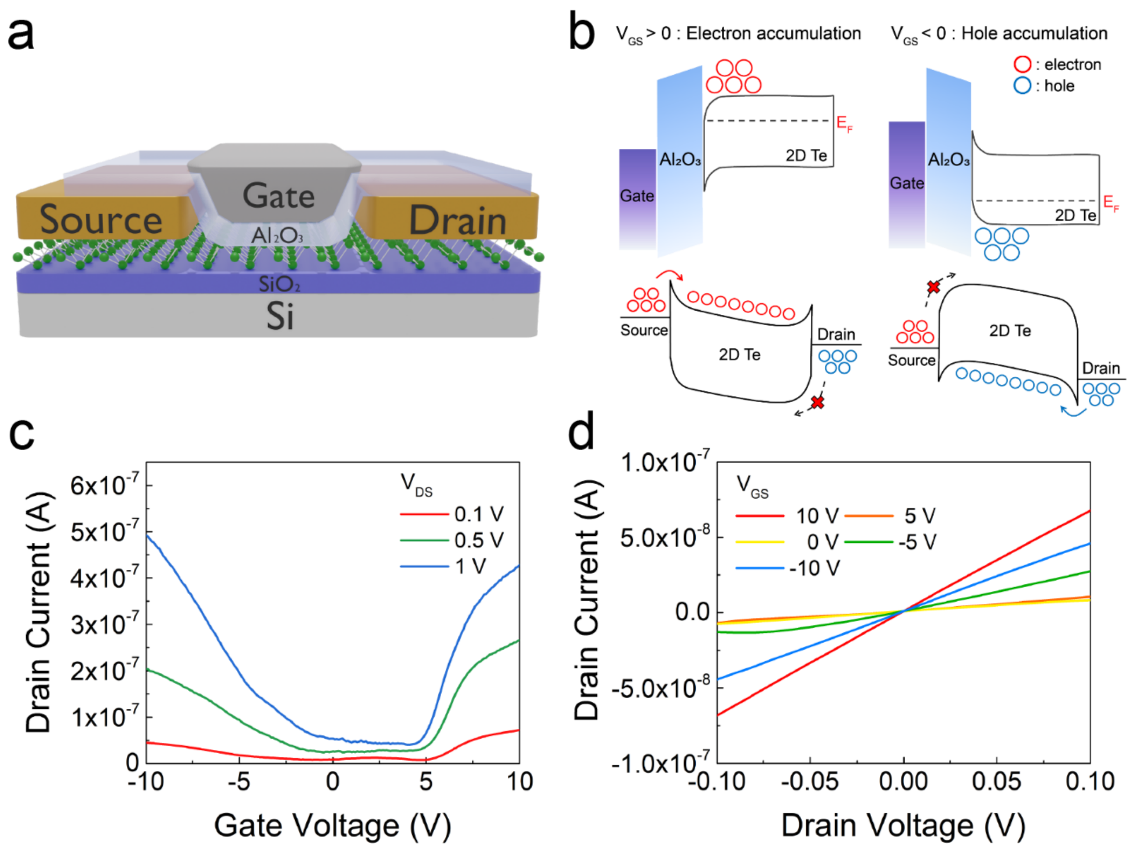


**Figure S7.** Electrical characteristics of an ambipolar Te top-gate transistor. (a) Schematic of the ambipolar Te synaptic device. (b) Schematic band diagram of 2D Te/$Al_2O_3$ at different gate biases. (c) Transfer curves and (d) output curves of ambipolar Te/$Al_2O_3$ FET.

To verify the feasibility of the ambipolar 2D Te transistor as an artificial synaptic device, its electrical characteristics were investigated, as shown in **Figure S7**. **Figure S7a** shows the schematic of an ambipolar 2D Te FET functioning as the ambipolar modulation layer in a top-gate structure. By depositing a 20 nm $Al_2O_3$ thin film *via* ALD, an n-doping effect was induced in the Te channel through oxygen vacancies at the Te/$Al_2O_3$ interface. Further, the dissociated methyl groups from the trimethylaluminum precursor during ALD can transfer electrons, increasing the electron concentration in Te.[1, 2] The change in the electron concentration in Te owing to the $Al_2O_3$ passivation layer can alter the energy position of the Fermi level, resulting in a band alignment different from that of bare 2D Te (**Figure S7b**). Following $Al_2O_3$ passivation, the Fermi level shifted towards the conduction band owing to the n-doping effect, causing electrons to accumulate in the 2D Te when a positive $V_{GS}$ is applied, rendering the n-doped Fermi level closer to the conduction band.[3] As a result, the energy band shifted downward, which allowed electron accumulation and reduced the Schottky barrier height (SBH), thereby facilitating electron carrier movement. In this case, the device operated as an n-type FET. Similarly, when a negative $V_{GS}$ was applied, the Fermi level became p-doped closer to the valence band, causing downward band bending and reducing the SBH, thus facilitating hole carrier movement. In this case, the device operated as a p-type FET. Consequently, 2D Te/$Al_2O_3$ can operate as an ambipolar transistor under various $V_{GS}$ values depending on band bending.

**Figure S7c** shows the ambipolar transfer characteristics of the 2D Te FET following $Al_2O_3$ deposition at various drain voltages. At $V_{DS}$ of 1 V, the region between the 0–5 V gate voltage was observed as the charge neutral point (CNP), with threshold voltages ($V_{TH}$) of 4.65 and -2.3 V in n- and p-type, respectively. This indicated the successful modification into ambipolar characteristics *via* a thermal ALD process. The symmetrical linear operation of the output curves, as shown in **Figure S7d,** indicated that ohmic contacts were well formed at both polarities. These results confirm the successful modulation of ambipolar behavior in the 2D Te transistor after $Al_2O_3$ deposition.

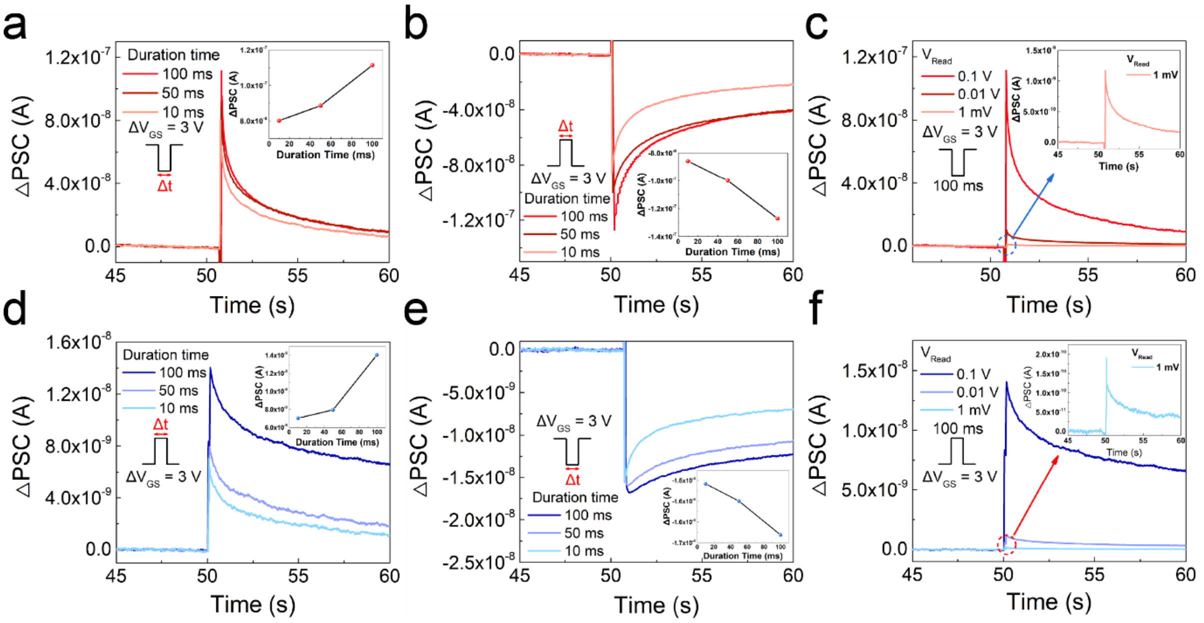


**Figure S8.** Gate terminal was modified to show short-term synaptic plasticity (STP) characteristics. N-type STP characteristics of (a) EPSC and (b) IPSC under different time durations of 10, 50, and 100 ms (read voltage: 0.1 V, amplitude: 3 V); inset: EPSC and IPSC change curves under different pulses. (c) EPSC curve under different read voltages of 1, 10, and 100 mV (amplitude: 3 V, time duration: 100 ms); inset: enlarged EPSC curve with a read voltage of 1 mV. P-type STP characteristics of (d) EPSC and (e) IPSC under different time durations of 10, 50, and 100 ms (read voltage: 0.1 V, amplitude: 3 V); inset: EPSC and IPSC change curves under different pulses. (f) EPSC curve under different read voltages of 1, 10, and 100 mV (amplitude: 3 V, time duration: 100 ms); inset: enlarged EPSC curve with a read voltage of 1 mV.

**Table S2.** Gate tunability performance summary of an ambipolar 2D Te synaptic transistor in terms of linearity, dynamic ranges, asymmetry ratio, and effective states.

| | Potentiation nonlinearity | Depression nonlinearity | Dynamic ranges ($G_{max}/G_{min}$) | Asymmetry ratio | Effective conductance states |
|---|---|---|---|---|---|
| Figure 3b | 1.17 | 1.66 | 4.49 | 0.28 | 100 |
| Figure 3e | 2.00 | 0.57 | 1.77 | 0.26 | 83 |

**Table S3.** Performance comparison of previously reported 2D material-based synaptic device.

| Active materials | Structure | Polarity | Oxide | Oxide Thickness | Power | Nonlinearity | Recognition accuracy | Ref |
|---|---|---|---|---|---|---|---|---|
| Te | Top-gate FET | Ambipolar (N-type) | $Al_2O_3$ | 20 nm | 3.5 fJ | 1.17/1.66 | 94.2% | This work |
| Te | Top-gate FET | Ambipolar (P-type) | $Al_2O_3$ | 20 nm | 19 fJ | 2.00/0.57 | 94.7% | This work |
| $MoS_2$ | Back-gate FET | Unipolar (N-type) | $SiO_2$ | 90 nm | 450 pJ | -1.3/-5.2 | 91.1% | [4] |
| $MoS_2$ | Back-gate FET | Unipolar (N-type) | $Al_2O_3$ | 35 nm | ~6 pJ | 1.84/0.86 | ~94.2% | [5] |
| $\alpha$-$In_2Se_3$ | Back-Gate FET | Unipolar (N-type) | $Ta_2O_3$ | 40 nm | 10 pJ | 0.81/2.1 | 93% | [6] |
| $WSe_2$ | Back-gate FET | Unipolar (P-type) | h-BN | 37.5 nm | ~532 fJ | 1.4/1.4 | ~90% | [7] |
| Nb-doped $WSe_2$ | Back-gate FET | Unipolar (P-type) | $SiO_2$ | 100 nm | 12.27 pJ | 0.01/5.88 | 91.3% | [8] |
| $WSe_2$ | Bottom gate FET | Ambipolar (hybrid) | $Al_2O_3$ | 15 nm | - | 2.2/2.1 | ~90% | [9] |
| $MoTe_2$ | Top-gate FET | Ambipolar | P(VDF-TrFE) | ~150 nm | - | 4.88/5.23 | ~88% | [10] |
| PDPPBTT/ZnO | Back-gate FET | Ambipolar | $SiO_2$ | 100 nm | - | - | 54 %/61% | [11] |
| $WSe_2$/h-BN/$MoTe_2$ | Back-gate FET | Ambipolar | $SiO_2$ | 300 nm | 900 fJ | 2/-1.5, -0.3/-0.45 | ~92% | [12] |

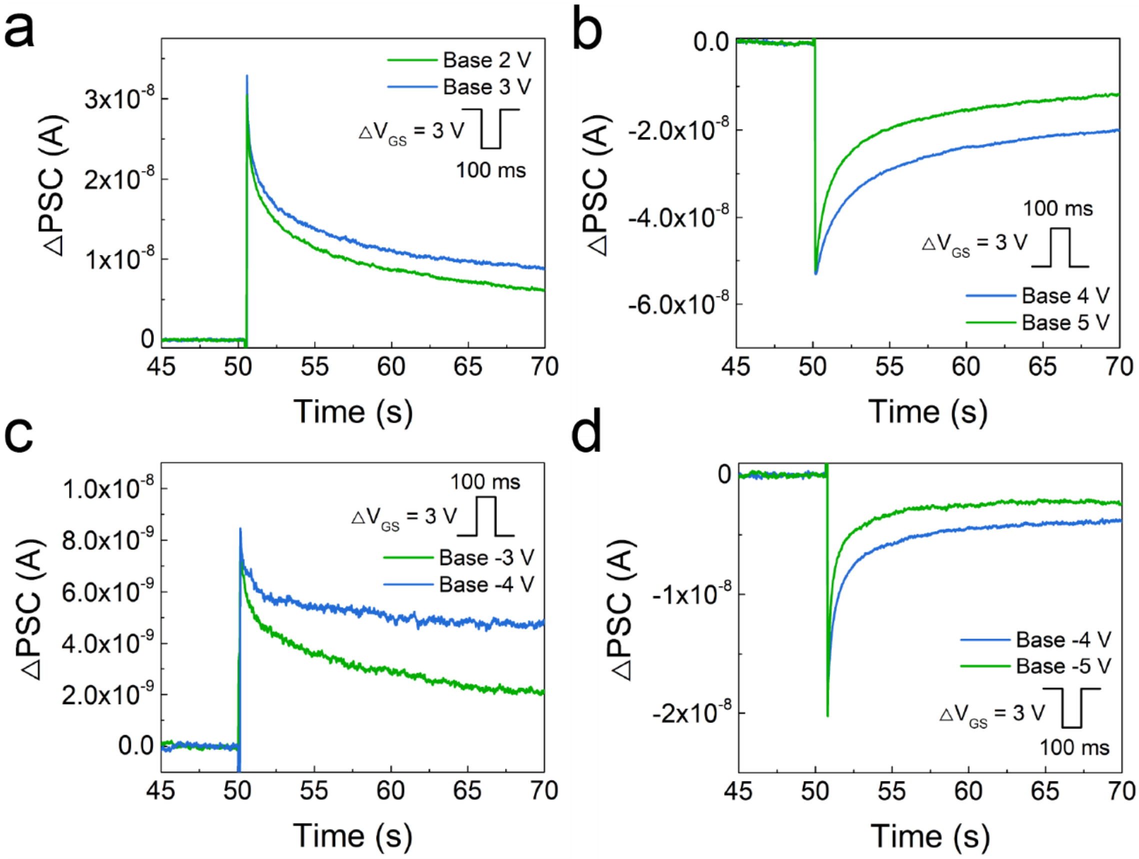


**Figure S9.** Retention characteristics were modified by adjusting the base of the input pulses of the artificial synaptic transistor. For the n-type 2D Te FET, (a) EPSC curves with bases at 2 and 3 V and (b) IPSC curves with bases at 4 and 5 V (read voltage: 0.1 V, amplitude: 3 V, time duration: 100 ms). For the p-type 2D Te FET, (c) EPSC curves with bases at -3 and -4 V and (d) IPSC curves with bases at -4 and -5 V (read voltage: 0.1 V, amplitude: 3 V, time duration: 100 ms).

## REFERENCES


1. A. Leonhardt, D. Chiappe, V. V. Afanas' ev, S. El Kazzi, I. Shlyakhov, T. Conard, A. Franquet, C. Huyghebaert and S. De Gendt, *ACS applied materials & interfaces*, 2019, **11**, 42697-42707.

2. A. Valsaraj, J. Chang, A. Rai, L. F. Register and S. K. Banerjee, *2D Materials*, 2015, **2**, 045009.

3. Y.-M. Chang, S.-H. Yang, C.-Y. Lin, C.-H. Chen, C.-H. Lien, W.-B. Jian, K. Ueno, Y.-W. Suen, K. Tsukagoshi and Y.-F. Lin, *Advanced Materials*, 2018, **30**, 1706995.

4. S. Oh, J.-J. Lee, S. Seo, G. Yoo and J.-H. Park, *npj 2D Materials and Applications*, 2021, **5**, 95.

5. J. H. Nam, S. Oh, H. Y. Jang, O. Kwon, H. Park, W. Park, J. D. Kwon, Y. Kim and B. Cho, *Advanced Functional Materials*, 2021, **31**, 2104174.

6. N. Mohta, A. Rao, N. Remesh, R. Muralidharan and D. N. Nath, *RSC advances*, 2021, **11**, 36901-36912.

7. S. Seo, S.-H. Jo, S. Kim, J. Shim, S. Oh, J.-H. Kim, K. Heo, J.-W. Choi, C. Choi and S. Oh, *Nature Communications*, 2018, **9**, 5106.

8. J. Bak, S. Kim, K. Park, J. Yoon, M. Yang, U. J. Kim, H. Hosono, J. Park, B. You and O. Kwon, *ACS Applied Materials & Interfaces*, 2023, **15**, 39539-39549.

9. Y. Gong, P. Xie, X. Xing, Z. Lv, T. Xie, S. Zhu, H. H. Hsu, Y. Zhou and S. T. Han, *Advanced Functional Materials*, 2023, **33**, 2303539.

10. Z.-D. Luo, S. Zhang, Y. Liu, D. Zhang, X. Gan, J. Seidel, Y. Liu, G. Han, M. Alexe and Y. Hao, *ACS nano*, 2022, **16**, 3362-3372.

11. Y. Wang, Q. Liao, D. She, Z. Lv, Y. Gong, G. Ding, W. Ye, J. Chen, Z. Xiong and G. Wang, *ACS applied materials & interfaces*, 2020, **12**, 15370-15379.

12. C. Yao, G. Wu, M. Huang, W. Wang, C. Zhang, J. Wu, H. Liu, B. Zheng, J. Yi and C. Zhu, *ACS Applied Materials & Interfaces*, 2023, **15**, 23573-23582.